nanomaterials

MDPI

Article

Effect of Calcination Temperatures on Surface Properties of Spinel $ZnAl_2O_4$ Prepared via the Polymeric Citrate Complex Method—Catalytic Performance in Glycerolysis of Urea

Nhiem Pham-Ngoc [1], Huy Nguyen-Phu [2] and Eun Woo Shin [1,*]

[1] School of Chemical Engineering, University of Ulsan Daehakro 93, Nam-gu, Ulsan 44610, Republic of Korea; nhiem.phamngoc@gmail.com
[2] Department of Chemical and Biomolecular Engineering, Seoul National University of Science and Technology, Seoul 01811, Republic of Korea; huycanphu@gmail.com
* Correspondence: ewshin@ulsan.ac.kr; Tel.: +82-52-259-2253

Abstract: In this study, we investigated urea glycerolysis over $ZnAl_2O_4$ catalysts that were prepared by using a citrate complex method and the influence of calcination temperatures on the surface properties of the prepared catalysts by varying the calcination temperature from 550 °C to 850 °C. As the reciprocal substitution between Al^{3+} and Zn^{2+} cations led to the formation of a disordered bulk $ZnAl_2O_4$ phase, different calcination temperatures strongly influenced the surface properties of the $ZnAl_2O_4$ catalysts, including oxygen vacancy. The increase in the calcination temperature from 550 °C to 650 °C decreased the inversion parameter of the $ZnAl_2O_4$ structure (from 0.365 to 0.222 for AlO_4 and 0.409 to 0.358 for ZnO_6). The disordered $ZnAl_2O_4$ structure led to a decrease in the surface acidity. The $ZnAl_2O_4$-550 catalyst had a large specific surface area, along with highly disordered surface sites, which increased surface acidity, resulting in a stronger interaction of the Zn NCO complex on its surface and an improvement in catalytic performance. Fourier transform infrared and thermogravimetric analysis results of the spent catalysts demonstrated the formation of a greater amount of a solid Zn NCO complex over $ZnAl_2O_4$-550 than $ZnAl_2O_4$-650. Consequently, the $ZnAl_2O_4$-550 catalyst outperformed the $ZnAl_2O_4$-650 catalyst in terms of glycerol conversion (72%), glycerol carbonate yield (33%), and byproduct formation.

Keywords: partially inverse spinel; polymeric citrate complex method; acidity; glycerol carbonate

Citation: Pham-Ngoc, N.; Nguyen-Phu, H.; Shin, E.W. Effect of Calcination Temperatures on Surface Properties of Spinel $ZnAl_2O_4$ Prepared via the Polymeric Citrate Complex Method—Catalytic Performance in Glycerolysis of Urea. *Nanomaterials* **2023**, *13*, 1901. https://doi.org/10.3390/nano13131901

Academic Editor: Antonio Guerrero-Ruiz

Received: 25 May 2023
Revised: 15 June 2023
Accepted: 19 June 2023
Published: 21 June 2023

1. Introduction

In recent years, climate change has become increasingly severe, which has led to the promotion of the development of the biodiesel industry [1,2]. Large amounts of crude glycerol as a byproduct generated from biodiesel production have an economic impact as a cheap and commercially viable renewable feedstock [3]. Among various glycerol reaction pathways, glycerolysis into glycerol carbonate (GC) is an interesting research direction. GC is an important glycerol derivative that is considered an interesting value-added chemical due to its excellent properties such as being a non-hazardous low-vapor pressure liquid, as well as its biodegradability, its low toxicity, its non-flammability, its high boiling point, and its low volatility [4–6]. Because of its outstanding properties, GC has a wide range of applications, including solvents, electrolytes, surfactants, wetting agents, and as a chemical intermediate in polymer synthesis [5,7].

Traditionally, the chemical synthesis of GC is by glycerol reacting with phosgene; however, this reaction is very dangerous and not environmentally friendly [8]. Alternatively, carbonate sources with milder reaction conditions such as dialkyl carbonate [9–11], alkylene carbonate [12], and CO_2 [13,14] can be used. With special advantages such as being cheap, easy to obtain, and recyclable, urea is used, along with glycerol, to efficiently produce GC [15–18]. In our previous studies, catalytic performance was affected by the existence

of Zn-containing intermediates, namely, zinc diamine diisocyanate ($Zn(NH_3)_2(NCO)_2$, abbreviated as a Zn NCO complex). The formation of the solid Zn NCO complex on the $ZnAl_2O_4$ phase offered many benefits for increasing the GC yield: acting as active sites for the heterogeneous GC pathway and interacting with an insoluble $ZnAl_2O_4$ phase [17].

The $ZnAl_2O_4$ spinel structure is represented with the typical formula $(Zn^{2+})[Al^{3+}{}_2]O_4$, where Zn^{2+} cations occupy one-eighth of the tetrahedral sites, and Al^{3+} cations occupy half of the octahedral sites. However, a normal $ZnAl_2O_4$ spinel structure can be partially disordered, replacing some Al^{3+} cations with Zn^{2+} cations in the octahedral sites and some Zn^{2+} cations with Al^{3+} cations in the tetrahedral sites [16]. It has been reported that the disordered structure of the $ZnAl_2O_4$ spinel structure affected the formation of the Zn NCO complex. Despite many studies on the various types of reactions or methods for preparing the $ZnAl_2O_4$ spinel structure, only a few studies have been conducted to investigate the influence of calcination temperatures on the structural properties of $ZnAl_2O_4$ catalysts. The formation of the disordered $ZnAl_2O_4$ structure is highly dependent on the calcination temperature.

Hence, in this work, $ZnAl_2O_4$ spinel catalysts with a disordered structure (denoted as $ZnAl_2O_4$-X, where X represents calcination temperature in °C) were prepared by using a polymeric citrate complex method and calcined at different temperatures ranging from 550 °C to 850 °C to investigate the influence of calcination temperatures on the $ZnAl_2O_4$ spinel lattice structure, the acidity of the catalysts, and the formation of a solid Zn NCO complex on the catalysts. We also used the prepared catalysts in the glycerolysis of urea under vacuum (3 kPa) at 140 °C for 5 h. Characterizations, including Fourier transform infrared spectroscopy (FT-IR) and X-ray photoelectron spectroscopy (XPS), were employed to observe the disordered $ZnAl_2O_4$ spinel structure. Acidic sites were measured via the temperature-programmed desorption of NH_3 (NH_3-TPD), and the formation of a solid Zn NCO complex was demonstrated by FT-IR and thermogravimetric analysis (TGA).

2. Materials and Methods

2.1. Catalyst Preparation

Citrate complex $ZnAl_2O_4$ catalysts were prepared by using a modified citrate complex technique [19]. An aqueous solution of $Zn(NO_3)_2.6H_2O$ (Sigma-Aldrich Korea, Gyounggi, Republic of Korea) and $Al(NO_3)_3 \cdot 9H_2O$ (Sigma-Aldrich Korea) with a molar ratio of Zn and Al in the precursor of 1:2 was prepared at room temperature, and the citric acid powder (citric acid to metal ratio of 2:1) (Sigma-Aldrich Korea) was added to the solution, followed by stirring with a magnetic bar. Stirring was continued at 70 °C to evaporate water until a yellow viscous gel solution was formed. The gel was further dried in an oven at 140 °C and spontaneously solidified by the emission of NO_x gases. Finally, all catalysts were calcined under a set temperature (550 °C–850 °C) in a furnace for 4 h. The catalysts were denoted as $ZnAl_2O_4$-X, where X indicates the calcination temperature.

2.2. Reaction Test

The reaction was performed in a round-bottom, three-neck 100 mL flask, in which one neck was connected to a vacuum line through a water condenser. Glycerol (Sigma-Aldrich Korea) (0.2 mol) was added to the flask at 80 °C under stirring by a magnetic bar to reduce the high viscosity of the glycerol. The reactor was connected to a vacuum pump through a HNO_3 (Sigma-Aldrich Korea) solution trap (to remove NH_3) and a cold trap (to remove order volatiles). After 10 min, 0.2 mol of urea (Sigma-Aldrich Korea) was poured into the flask to mix with glycerol in the solution. When all the urea was dissolved completely in glycerol and the solution was transparent, a certain amount of catalyst (5 wt% compared with the initial glycerol amount) was added to the flask. The reaction was performed under vacuum pressure (3 kPa) at 140 °C with constant stirring.

After the reaction tests, ethanol (Sigma-Aldrich Korea) was poured into the final products, and the liquid products were separated from the spent catalyst via filtration. The liquid product was quantitatively analyzed via gas chromatography by using a gas

chromatography machine (Acme 6100 GC, YL Instrument Co., Ltd., Dongangu, Anyang, Republic of Korea) (a schematic diagram of the catalyst activity test device is shown in Figure S1 in the Supplementary material) with a flame ionization detector and a capillary column DB-Wax (30 m × 0.25 mm × 0.25 μm). The molar amount of each component was calculated by using the internal standard method, with tetraethylene glycol (Sigma-Aldrich Korea) as the internal standard chemical. Glycerol conversion, GC selectivity, GC yield, and byproduct selectivity were calculated by using the equations below. The amount of each chemical is on the mole unit.

$$\text{Glycerol conversion } (\%) = \frac{\text{Initial amount of glycerol} - \text{Residual amount of glycerol}}{\text{Initial amount of glycerol}} \times 100$$

$$\text{GC yield } (\%) = \frac{\text{AmountofGC}}{\text{Initial amount of glycerol}} \times 100$$

$$\text{GC selectivity } (\%) = \frac{\text{GC yield } (\%)}{\text{Glycerol conversion } (\%)} \times 100$$

$$\text{Byproduct selectivity } (\%) = \frac{\text{Amount of byproduct}}{\text{Initial amount of glycerol} - \text{Residual amount of glycerol}} \times 100$$

FT-IR spectra of the liquid products were obtained by using a Thermo Scientific™ Nicolet™ iS™5 FT-IR spectrometer (Thermo Fisher Scientific, Waltham, MA, USA) by dropping a liquid sample between KBr (Sigma-Aldrich Korea) plates.

2.3. Catalyst Characterization

The Chemical Composition Zn/Al Molar Ratio was measured by using an Agilent Technologies 5110 ICP-OES (Agilent, Santa Clara, CA, USA) instrument. The surface characterizations were measured via N_2 adsorption isotherm analysis on a Micromeritics ASAP 2020 (USA) apparatus. The surface area was calculated by using the Brunauer–Emmett–Teller (BET) method. X-ray diffraction (XRD) patterns for fresh catalysts were obtained by using a Rigaku RAD-3C diffractometer (Rigaku Corp., Tokyo, Japan) with Cu Ka radiation (λ = 1.5418 Å) at a scattering angle (2θ) scan rate of 2°/min, operating at 35 kV and 20 mA. The fresh and spent catalysts were analyzed by using a Thermo Scientific Nicolet iS5 FT-IR spectrometer (Thermo Fisher Scientific). XPS data were surveyed by using a Thermo Scientific K-Alpha XPS spectrometer (Thermo Fisher Scientific). The numbers of acidic and basic sites were measured on the basis of TPD-NH_3/CO_2 on a MicrotracBEL BELCAT-M instrument (MicrotracBEL Corp., Osaka, Japan). An amount of 100–200 mg of fresh catalysts was placed into the quartz sample tube of the instrument. Initially, the sample was pretreated under helium flow (100 mL/min) at 600 °C for 1 h and then cooled down to 50 °C. After that, a flow of NH_3 or CO_2 (50 mL/min) was injected for chemisorption. Finally, the temperature was increased to 600 °C with a ramping rate of 1.5 °C/min; the desorbed species were removed via helium flow (30 mL/min) and analyzed via thermal conductivity detection. The TGA of the spent catalysts was performed by using a TGA Q50 apparatus (TA Instruments, New Castle, DE, USA).

3. Results and Discussion

3.1. Characterizations of Fresh Catalysts

The textural properties of the fresh catalysts, which were calculated from N_2 adsorption–desorption measurements, are summarized in Table 1, and the N_2 adsorption–desorption isotherms and pore size distributions are shown in Figure S2. As indicated in Figure S2a, all $ZnAl_2O_4$ catalysts exhibited type IV isotherm and type H3 hysteresis loops (based on the IUPAC classification [20]), which is typical for mesoporous materials, indicating slit-shaped pores. As the calcination temperature increased, the hysteresis loop became narrower, with a lower BET surface area and a lower average pore volume in the order of $ZnAl_2O_4$-850 < $ZnAl_2O_4$-750 < $ZnAl_2O_4$-650 < $ZnAl_2O_4$-550. In contrast, the average pore diameter exhibited an opposite trend. Increasing the calcination temperature led to

the collapse of small pores to generate bigger ones. The relationships between textural properties and calcination temperatures are depicted in Figure 1.

Table 1. Textural properties, $ZnAl_2O_4$ crystallite sizes, and the degree of orderliness of the $ZnAl_2O_4$ spinel of fresh catalysts.

Catalyst	Textural Properties			Chemical Composition	Order Parameter [c]	$ZnAl_2O_4$ Crystallite Size (nm) [d]
	S_{BET} (m^2/g) [a]	V_{pore} (cm^3/g) [a]	D_{pore} (nm) [a]	Zn/Al Molar Ratio [b]		
$ZnAl_2O_4$-550	37.65	0.21	14.09	2.07	0.4784	20.29
$ZnAl_2O_4$-650	25.29	0.14	15.31	2.10	0.4922	25.50
$ZnAl_2O_4$-750	19.17	0.11	16.87	2.11	0.5074	29.21
$ZnAl_2O_4$-850	9.45	0.10	27.16	2.06	0.5153	34.06

[a] Measured via N_2 isothermal adsorption–desorption at 77 K; surface area was calculated with BET method; pore volume and pore size were obtained with the BJH method. [b] Determined from ICP-OES. [c] Calculated via the fraction intensity of $ZnAl_2O_4$ (331) and [$ZnAl_2O_4$ (331) + $ZnAl_2O_4$ (400)] from XRD patterns. [d] Calculated via Debye–Scherrer equation applied to XRD $ZnAl_2O_4$ (311) peak.

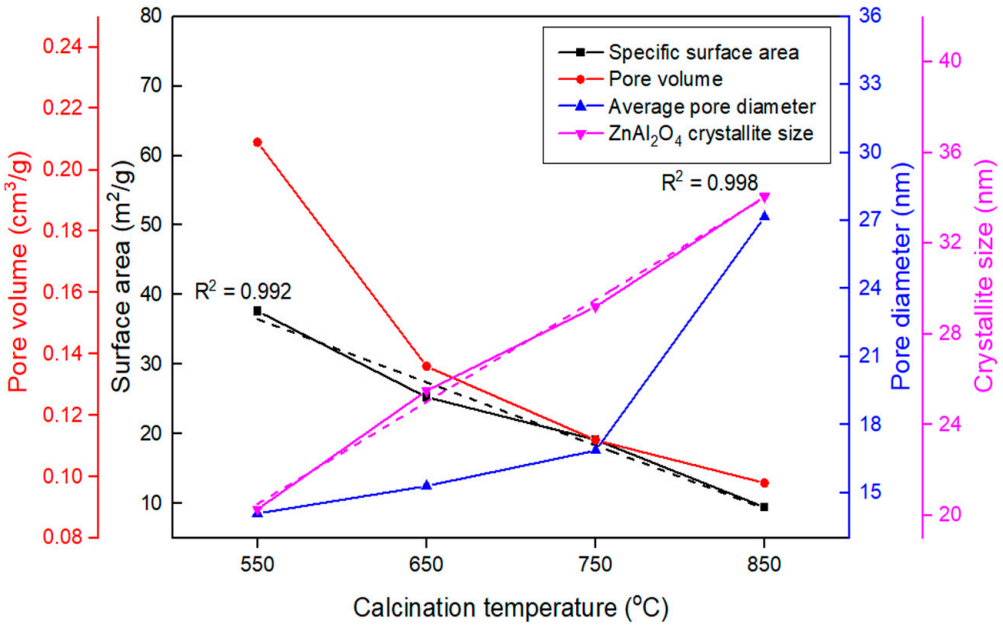

Figure 1. Relationship between textural properties and calcination temperatures.

Figure 2 depicts the XRD patterns of the fresh $ZnAl_2O_4$-X catalysts. Characteristic peaks appearing at 2θ = 31.2°, 36.8°, 44.8°, 49.1°, 55.7°, 59.3°, 65.2°, 74.1°, and 77.3° can be attributed to the crystalline phase of $ZnAl_2O_4$. All XRD patterns show $ZnAl_2O_4$ peaks, which indicates the formation of $ZnAl_2O_4$ crystallite after high-temperature calcination by using the polymeric citrate complex method. The final decomposition temperature of the precursor in the derivative TGA (DTGA) result is below 550° (Figure S3), confirming that the $ZnAl_2O_4$ crystallite structure is completely formed at a calcination temperature above 550 °C. With increasing calcination temperature, the characteristic diffraction peaks become sharper, narrower, and more intensive, indicating an increase in the crystallinity and particle size of $ZnAl_2O_4$.

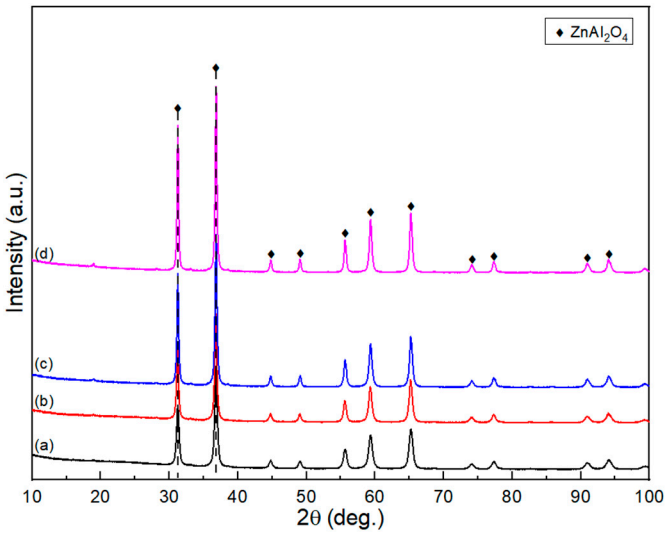

Figure 2. XRD patterns of fresh catalysts: (a) $ZnAl_2O_4$-550, (b) $ZnAl_2O_4$-650, (c) $ZnAl_2O_4$-750, and (d) $ZnAl_2O_4$-850.

In addition, the average crystallite size (D) of single-phase spinel samples can be estimated by using the Debye–Scherrer equation [21,22]:

$$D = \frac{0.9\lambda}{\beta Cos\theta},$$

where D represents the average crystallite size, λ denotes the wavelength of the X-ray source (Cu Kα, 1.54 Å), β denotes the integral breadth of the (311) diffraction peak, and θ denotes the Bragg's diffraction angle. The calculated results are presented in Table 1. In normally ordered spinel structures, the intensity of all odd reflections (e.g., 331) shows higher intensity than those of all even reflections (e.g., 400). The XRD peak intensities of (400) and (331) for various calcination temperatures are shown in Figure S4. It was observed that the peak intensities of (400) and (331) changed significantly with increasing calcination temperature. The degree of the order parameter in spinel samples can be calculated by using the following equation [23]:

$$\Delta I = \frac{I_o}{I_o + I_e},$$

where I_o and I_e denote intensities corresponding to odd and even reflections, respectively. The disordered spinel phase can be formed because some fraction of Al^{3+} cations occupies the tetrahedral site, and Zn^{2+} cations occupy the octahedral site [24,25]. The degree of the order parameter in the spinel samples is shown in Table 1. The order parameters of $ZnAl_2O_4$-550 and $ZnAl_2O_4$-650 are 0.4784 and 0.4922, respectively. These values prove that the $ZnAl_2O_4$ spinel structure obtained at the calcination temperatures of 550 °C and 650 °C is a disordered structure, where Al^{3+} exists in tetrahedral positions and Zn^{2+} in octahedral positions. When the calcination temperature is raised above 750 °C, the degree of the order parameters is above 0.5, indicating that the $ZnAl_2O_4$ spinel is a normally ordered structure.

The FT-IR spectra of the fresh catalysts are shown in Figure 3A. The two vibration bands at 661 and 554 cm^{-1} can be attributed to the stretching mode of the octahedrally coordinated Al-O (AlO_6), with another assignment of the peak at 495 cm^{-1} to the bending mode of AlO_6. A broad shoulder band from 704 to 900 cm^{-1} can be assigned to tetrahedrally coordinated Al-O (AlO_4) [16,26–28]. The enlarged spectra (from 600 to 1000 cm^{-1}) focusing on the vibration bands of AlO_4 and AlO_6 are depicted in Figure 3B. The relative intensities of AlO_4 to AlO_6 decrease as the calcination temperature increases. The AlO_4 vibration bands for the $ZnAl_2O_4$-750 and $ZnAl_2O_4$-850 catalysts are weak. In contrast, the shoulder

of the AlO_4 vibration for $ZnAl_2O_4$-550 and $ZnAl_2O_4$-650 is strong and observable. The presence of Al^{3+} in the tetrahedral position reflects a partial inversion of the $ZnAl_2O_4$ spinel structure. The FT-IR results are consistent with the XRD results and the inversion parameter obtained from the XPS measurement, which is shown later.

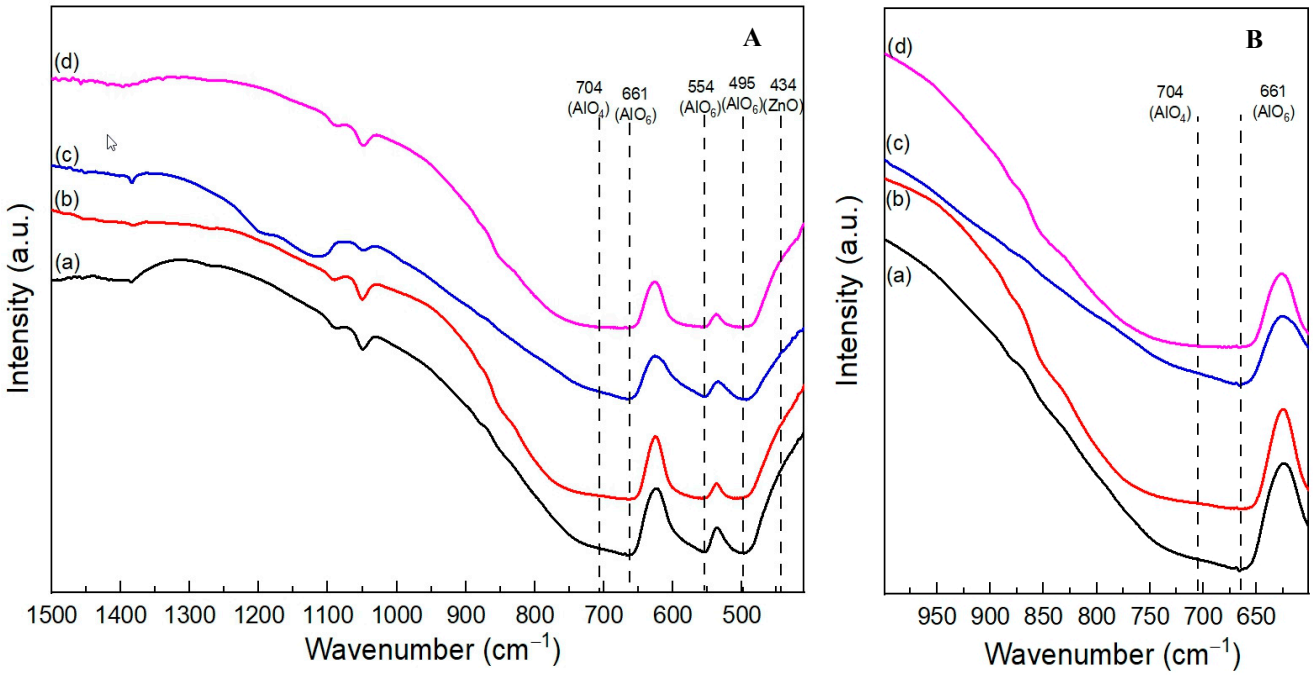

Figure 3. (**A**)FT-IR spectra of fresh catalysts: (a) $ZnAl_2O_4$-550, (b) $ZnAl_2O_4$-650, (c) $ZnAl_2O_4$-750, and (d) $ZnAl_2O_4$-850. (**B**) Enlarged FT-IR spectra.

The deconvoluted XPS results of the fresh $ZnAl_2O_4$-550 and $ZnAl_2O_4$-650 catalysts are depicted in Figure 4. The Al2p XPS spectrum is illustrated in Figure 4A. The peak at a binding energy of 71.0 eV can be assigned to Al^{3+} occupying the tetrahedral sites (AlO_4) [29], and a peak of approximately 74.2 eV can be assigned to Al^{3+} occupying the octahedral sites (AlO_6) [29–31]. In $Zn2p_{3/2}$ spectra, as shown in Figure 4B, the larger peak at a lower binding energy (approximately 1022–1022.2 eV) is attributed to Zn^{2+} occupying the tetrahedra sites (ZnO_4), and a smaller peak at a higher binding energy (approximately 1024.5 eV) is attributed to Zn^{2+} occupying the octahedra sites (ZnO_6) [29,30,32]. The normally ordered $ZnAl_2O_4$ spinel structure contains Al^{3+} cations at the octahedral sites and Zn^{2+} cations at the tetrahedral sites. When some Al^{3+} cations substitute Zn^{2+} cations in the tetrahedral positions and some Zn^{2+} cations substitute Al^{3+} cations in the octahedral positions, this results in the formation of a partially inversed spinel structure. The inversion parameter of a spinel structure can be defined by surface XPS measurements [30]. Table 2 shows the inversion parameter of the fresh $ZnAl_2O_4$-550 and $ZnAl_2O_4$-650 catalysts by calculating the ratio of $AlO_4/(AlO_4 + AlO_6)$ and $ZnO_6/(ZnO_4 + ZnO_6)$, and the inversion parameter values follow the order of $ZnAl_2O_4$-550 > $ZnAl_2O_4$-650. These results help us demonstrate that the degree of disorder of the spinel $ZnAl_2O_4$ structure decreases with increasing calcination temperature. The deconvoluted patterns of O1s can be fitted to three peaks. The peak O_a at the highest binding energy (approximately 543.5–534.8 eV) can be assigned to the oxygen weakly bonded with the surface of the catalysts (such as adsorbed H_2O and O_2 from the atmosphere) [16,33,34]. The peak at approximately 533.4–533.6 eV (O_b) can be assigned to the oxygen-deficient regions or oxygen vacancy (O_v) [33,34]. Finally, the peak at the lowest binding energy (approximately 531.4–531.7 eV) can be assigned to the lattice O in the $ZnAl_2O_4$ phase [16]. In a partially inversed spinel structure or a disordered structure, the substitution of a Zn^{2+} cation with an Al^{3+} cation to generate a Zn^{2+} octahedral site and Al^{3+} tetrahedral site is the main reason for the oxygen vacancy

formation on the catalyst surface. An oxygen vacancy was formed to balance the positive charge of the cation caused by the substitution of Zn^{2+} for Al^{3+} at an octahedral site. The intensities of oxygen vacancy follow the order of $ZnAl_2O_4$-550 > $ZnAl_2O_4$-650, which are listed in Table 2.

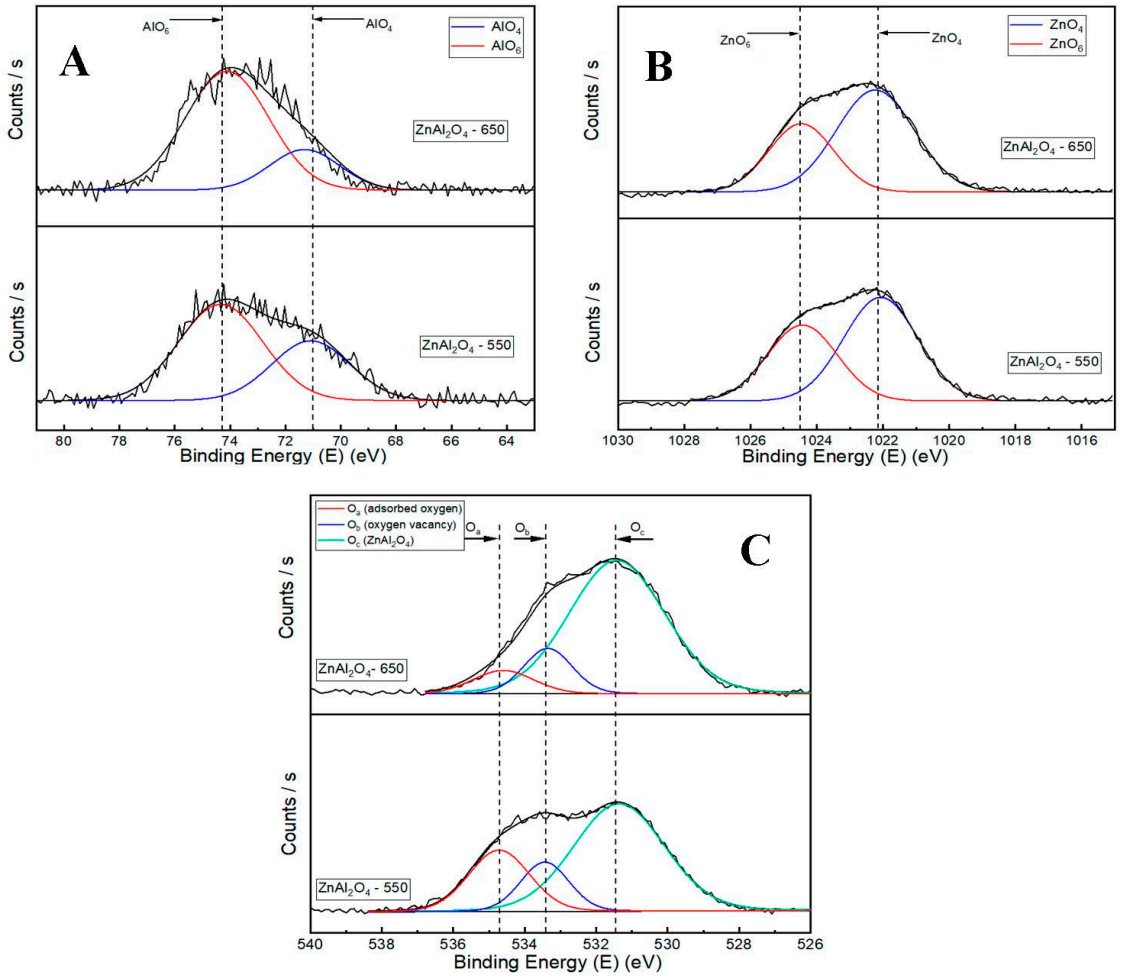

Figure 4. Deconvoluted XPS results of fresh catalysts: (**A**) Al2p XPS results, (**B**) $Zn2p_{3/2}$ XPS results, and (**C**) O1s XPS results.

Table 2. The change in the number of acidic sites and oxygen vacancy is based on the ratio of $AlO_4/(AlO_4 + AlO_6)$ and $ZnO_6/(ZnO_4 + ZnO_6)$.

Catalyst	Intensity Ratio of $AlO_4/(AlO_4 + AlO_6)$ [a]	Intensity Ratio of $ZnO_6/(ZnO_4 + ZnO_6)$ [b]	Acidic Sites (mmol/g)	The Fraction of O_b (%) [c]
$ZnAl_2O_4$-550	0.365	0.409	0.45	15.7
$ZnAl_2O_4$-650	0.222	0.358	0.32	13.6
$ZnAl_2O_4$-750	-	-	0.29	-
$ZnAl_2O_4$-850	-	-	0.1	-

[a] Intensity ratios of the AlO_4 (tetrahedral site) and AlO_6 (octahedral site) were obtained from the deconvolution of XPS results by using the Origin software (OriginPro 2021 9.8.0.200). [b] Intensity ratios of the ZnO_6 (octahedral site) and ZnO_4 (tetrahedral site) were obtained from the deconvolution of XPS results by using the Origin software. [c] The fraction of O_b was calculated via the percentage of intensity of O_b in total intensity of deconvolution O1s XPS results.

The NH_3-TPD measurements of the fresh catalysts are shown in Figure S5, and the acidic sites are summarized in Table 2. The number of acidic sites decreases in the order of $ZnAl_2O_4$-550 > $ZnAl_2O_4$-650 > $ZnAl_2O_4$-750 > $ZnAl_2O_4$-850. The relationship between the calcination temperature and the total number of acidic sites is shown in Figure 5.

In this study, the presence of AlO_4 and ZnO_6 in the $ZnAl_2O_4$ spinel structure indicates the partially disordered structure of the catalyst. Furthermore, the partially disordered structure $ZnAl_2O_4$ spinel is capable of producing surface acidity on catalysts, which is related to the XPS intensity of O_a (in Figure 4) [16]. The high-intensity peak of O_a in the $ZnAl_2O_4$-550 catalyst and its dependency on the calcination temperature follow the same trend as the number of acidic sites.

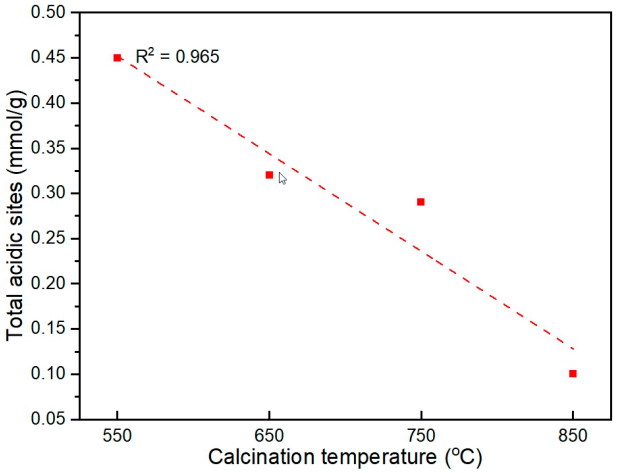

Figure 5. Relationship between total number of acidic sites and calcination temperatures.

The relationship between the number of acidic sites of the fresh catalysts and the inversion parameter (intensity ratio of $AlO_4/(AlO_4 + AlO_6)$), the XPS intensity of oxygen vacancies (O_v), and the inversion parameter (intensity ratio of $ZnO_6/(ZnO_4 + ZnO_6)$) are shown in Figure 6. In the normally ordered $ZnAl_2O_4$ spinel structure, Al^{3+} cations occupy the octahedral sites (AlO_6) with low acidity. Meanwhile, Al^{3+} cations occupying tetrahedral sites (AlO_4) in the partially inversed $ZnAl_2O_4$ spinel structure can result in higher surface acidity [16,27,35–38]. The higher Lewis acidity of AlO_4 than AlO_6 can be explained by the lower energy acceptor orbital of the AlO_4 sites. When AlO_4 contacts the surface, the removal of one of the four oxygen atoms results in the formation of three-coordinated Al with higher Lewis acidity strength [39]. Figure 6 depicts the positive relationship between the inversion parameter ($AlO_4/(AlO_4 + AlO_6)$) and total surface acidity. With an increase in the calcination temperature, the disordered $ZnAl_2O_4$ structure decreases, indicating that there are fewer sites in which Al^{3+} cations occupy the tetrahedral position (AlO_4), which decreases the total surface acidity. Another factor increasing surface acidity is the Lewis acidity of surface oxygen vacancies. Substitution of Zn^{2+} cations for Al^{3+} cations at the octahedral site and the formation of oxygen vacancies (O_v) to balance the positive charge of the cations can increase surface acidity. Mefford et al. [40] reported that the formation of surface hydroxyl groups was related to the Lewis acidity of surface oxygen vacancies, and evidence was provided from XPS O_a peaks of H_2O or O_2 adsorbed from the atmosphere. As the number of ZnO_6 sites decreases with increasing calcination temperature, fewer oxygen vacancies are formed, lowering the surface acidity of the $ZnAl_2O_4$-650 catalyst compared with the $ZnAl_2O_4$-550 catalyst. From the above findings, we conclude that at the calcination temperature of 550 °C, a partially disordered $ZnAl_2O_4$ spinel structure is formed, in which some Al^{3+} cations occupy tetrahedral positions, and Zn^{2+} occupy octahedral positions, resulting in the formation of oxygen vacancies, which increases the surface acidity of the catalyst. With increasing calcination temperature, the structure of $ZnAl_2O_4$ gradually returns to normal, and the number of AlO_4 and ZnO_6 sites and oxygen vacancies decreases, lowering the surface acidity of the catalyst.

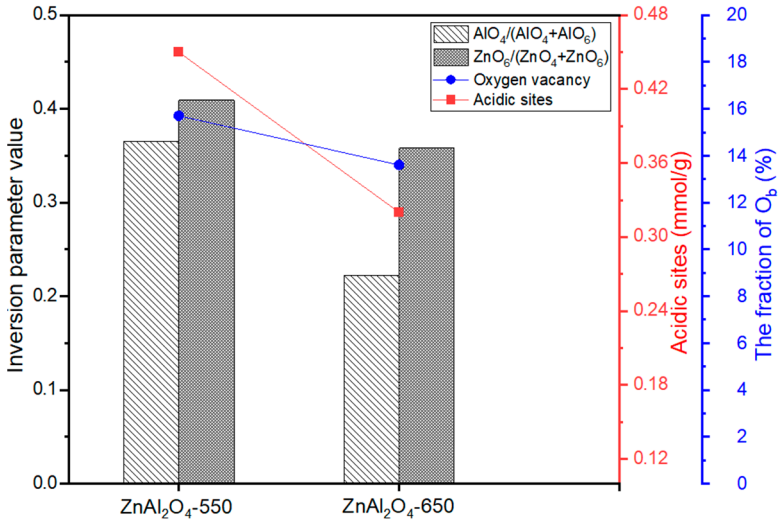

Figure 6. Relationship between the number of acidic sites vs. inversion parameter ($AlO_4/(AlO_4 + AlO_6)$) and O1s XPS intensity (oxygen vacancy) vs. inversion parameter ($ZnO_6/(ZnO_4 + ZnO_6)$).

3.2. Catalytic Activity

The reaction results (yield, conversion, and selectivity) calculated from gas chromatograms (a typical gas chromatogram is shown in Figure S6, see Supplementary Materials) for the glycerolysis of urea over the $ZnAl_2O_4$-550 and $ZnAl_2O_4$-650 catalysts are summarized in Table 3 and Figure 7A. During the reaction, besides the formation of the main product GC, there are also byproducts such as chemicals (2), (3), and (5). After the 5 h experiment, no other by-products are collected, indicating that the carbon balance between reagents and products is close to 100% (Table S1, see Supplementary Materials). The relationship between the number of acidic sites vs. GC yield and the number of basic sites (Figure S7, see Supplementary Materials) vs. byproduct (2) selectivity for each catalyst is depicted in Figure 7B. At a reaction time of 5 h, the $ZnAl_2O_4$-550 catalyst exhibited higher GC yield and lower (2) selectivity (GC yield = 46%, (2) selectivity = 34%) than the $ZnAl_2O_4$-650 catalyst with GC yield = 41% and (2) selectivity = 41%. Previous studies have reported the existence of the intermediate isocyanate (NCO) complex of Zn, which is an active site for the reaction [18,41]. Moreover, it has been proven that the Lewis acidic site acts as an active site for the ammonia (NH_3) group of Zn NCO complex adsorption [16]. The $ZnAl_2O_4$-550 catalyst has a higher GC yield and more surface acidic sites than the $ZnAl_2O_4$-650 catalyst.

Table 3. Analysis of liquid products obtained from the glycerolysis of urea over various mixed oxide catalysts prepared at different calcined temperatures. (Reaction temperature = 140 °C, reaction time = 5 h, reaction pressure = 3 kPa, glycerol/urea ratio = 1:1). (2): 2,3-dihydroxypropyl carbamate, (4): 4 (hydroxymethyl)oxazolidin-2-one, and (5): (2-oxo-1,3-dioxolan-4-yl) methylcarbamate.

Catalyst	Glycerol Conversion (%)	GC Yield (%)	Selectivity (%)				Acidic Sites (mmol/g)	Basic Sites (mmol/g)
			GC	(2)	(4)	(5)		
$ZnAl_2O_4$-550	72.2 ± 0.7	33 ± 0.3	45.8 ± 0.5	34.3 ± 0.1	12.4 ± 0.2	7.5 ± 0.1	0.45	0.23
$ZnAl_2O_4$-650	72.2 ± 0.8	30 ± 0.3	40.9 ± 0.7	40.9 ± 0.3	10.9 ± 0.2	7.3 ± 0.1	0.32	0.13

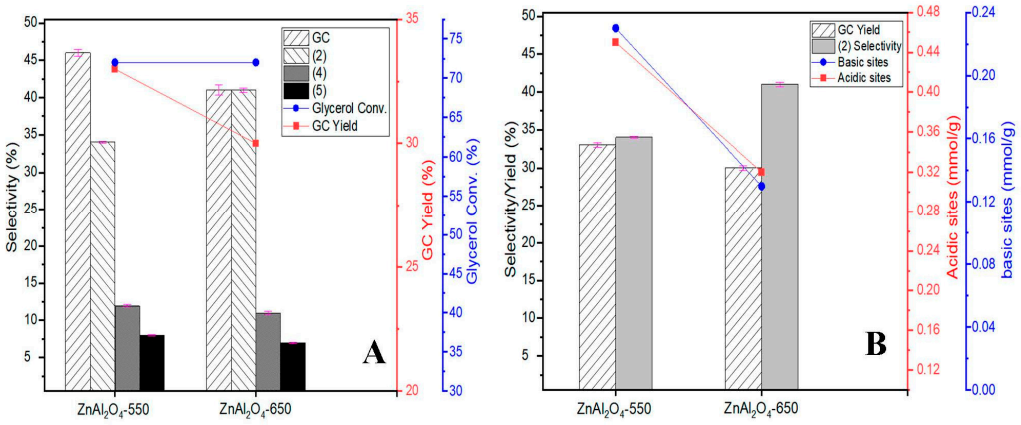

Figure 7. Catalytic performance of $ZnAl_2O_4$-550 and $ZnAl_2O_4$-650 catalysts in the glycerolysis of urea (**A**), and the relationship between the number of acidic sites vs. GC yield and the number of basic sites vs. (2) selectivity (**B**).

The formation of the Zn NCO complex on the solid phase can be confirmed by the FT-IR and TGA of the spent catalysts. The FT-IR spectra of the spent catalysts are shown in Figure 8. Besides the bands for AlO_4 and AlO_6 being detected at 704 and 661 cm^{-1}, respectively, the vibration band of NCO in the Zn NCO complex on the solid phase is detected at 2350 cm^{-1} [42]. There is no information about the NCO band in the fresh catalysts. However, after a 5 h reaction, this band can be detected by FT-IR. The intensity of the NCO peak for $ZnAl_2O_4$-550 is higher than that for $ZnAl_2O_4$-650 because of the higher number of acidic sites in this catalyst. The same trend is presented by TGA and DTGA profiles in Figure 9. The DTGA profiles of the spent catalysts (Figure 9B) show the decomposition of the Zn NCO complex at 273 °C for $ZnAl_2O_4$-550 and 254 °C for $ZnAl_2O_4$-650 [16]. The higher decomposition temperature for the $ZnAl_2O_4$-550 catalyst can be attributed to a stronger crystalline Zn NCO complex with higher thermal stability. The DTGA results are consistent with the FT-IR results. The higher intensity of the Zn NCO decomposition peak in $ZnAl_2O_4$-550 demonstrated that the ability to adsorb the ammonia group in the Zn NCO of AlO_4 (Lewis acidic site) is more significant in the $ZnAl_2O_4$-550 catalyst than in the $ZnAl_2O_4$-650 catalyst.

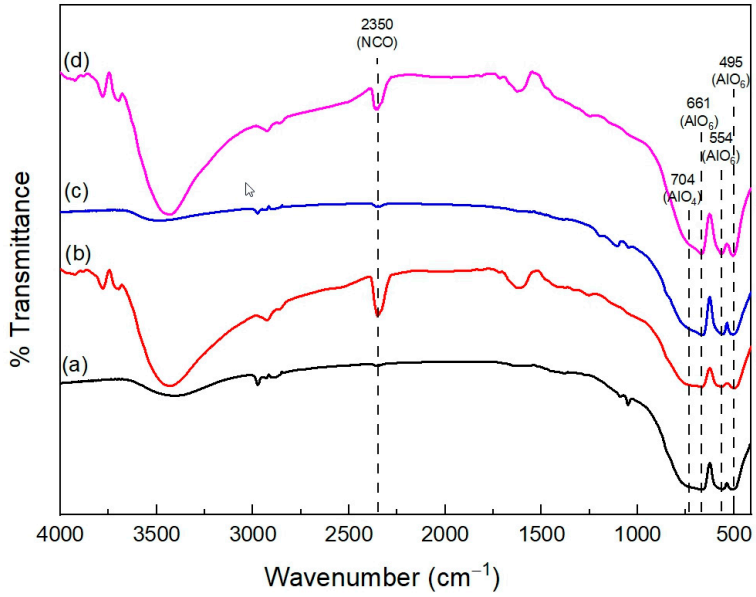

Figure 8. FT-IR results of fresh and spent catalysts: (a) $ZnAl_2O_4$-550 fresh, (b) $ZnAl_2O_4$-550 spent 5 h, (c) $ZnAl_2O_4$-650 fresh, and (d) $ZnAl_2O_4$-650 spent 5 h.

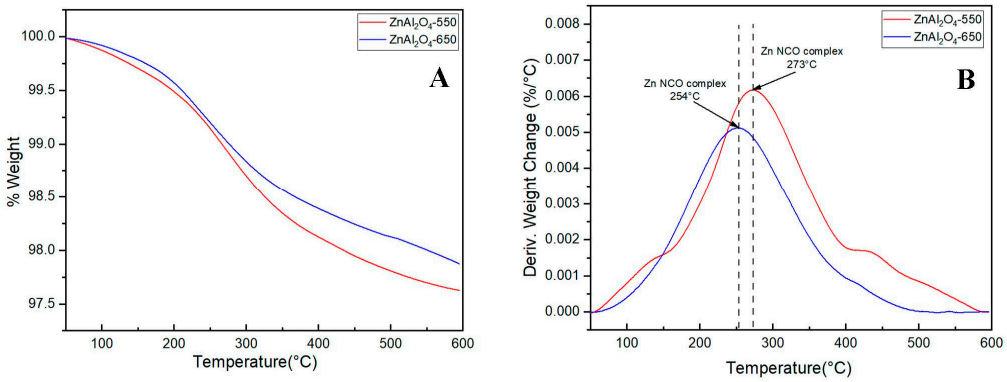

Figure 9. (**A**) TGA and (**B**) DTGA of spent catalysts after 5 h reaction.

Another notable finding is the relationship between surface basicity and byproduct (2) selectivity. The basic site values are shown in Table 3 and Figure 7B, showing that the relationship between the number of basic sites and (2) selectivity is inversely proportional. That is, if the number of basic sites decreases, more byproducts (2) are formed, and the GC yield reduces. Fernandes et al. [43] explained that surface basicity acted as an active site for the (2) byproduct decomposition process. This study shows the same trend: when using $ZnAl_2O_4$-550 with more basic sites for the reaction, (2) selectivity (34%) is lower, whereas it is higher with $ZnAl_2O_4$-650 (41%).

Catalytic reaction routes over a disordered $ZnAl_2O_4$ spinel structure are depicted in Scheme 1. As mentioned above, there are several disordered sites over a partially inverted $ZnAl_2O_4$ spinel: AlO_4 (symbolized as Al*), ZnO_6 (symbolized as Zn*) and oxygen vacancies (symbolized as O_v). $ZnAl_2O_4$ catalysis follows the heterogeneous reaction pathways. The catalysts form the Zn NCO complexes via the reaction with urea. The AlO_4 site works as a Lewis acidic site where the ammonia (NH_3) group of the Zn NCO complex can adsorb. The presence of the Zn NCO complex adsorbed on the solid phase is confirmed by the FT-IR and TGA measurements.

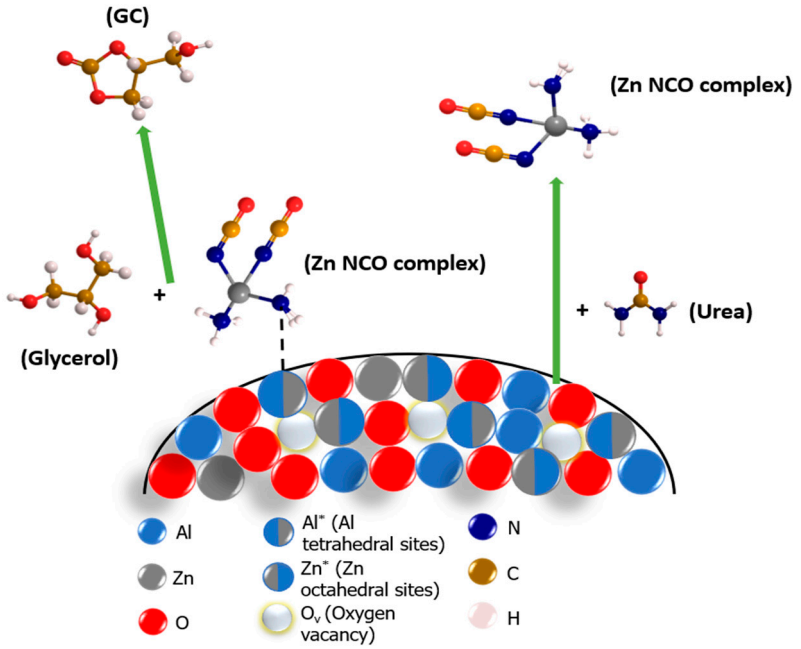

Scheme 1. An illustration of the reaction pathways involved in the urea-glycerol carbonylation on the surface of the disordered $ZnAl_2O_4$ spinel structure.

In Table 4, the catalytic reaction results in this work are compared to those recently published in the literature. Because the $ZnAl_2O_4$ catalyst follows only the heterogeneous catalysis pathway, the glycerol conversion and GC yield values are relatively low. However, it can still be compared with some previous studies. Zhang et al. prepared the zinc glycerolate (ZMG) and ZnO from zinc glycerolate (ZnO from ZMG) via the calcination method. Glycerol conversion and GC yield of the ZMG are about 65 and 55%, respectively. The authors have demonstrated through reaction tests that catalysts with acidic and basic properties favor the synthesis of glycerol carbonate.

Table 4. Summary of catalytic reaction performance of glycerol carbonylation with urea over several catalysts.

Catalyst	Mol Ratio Glycerol/Urea	Weight % Catalyst/Glycerol	Glycerol Conversion (%)	GC Yield (%)	Reference
ZnO pure	1:1.5	5	~60	~35	[44]
ZMG	1:1.5	5	~65	~55	[44]
Co_3O_4/ZnO	1:1.5	5	69	97	[45]
$La_2Cu_{0.5}Fe_{0.5}O_4$	1:1	5	49	82	[46]
$La(OH)_3$	1:1.5	5	42.3	55.6	[47]
MoO_3/SnO_2	1:3	10	69	97	[48]
MgO	1:1.5	-	71	100	[43]
ZnO	1:1.5	5	67	49	[49]
[HOEMIm][PF_6]	1:1.5	-	62	47	[50]
$ZnAl_2O_4$-550	1:1.5	5	72.2	33	This work
$ZnAl_2O_4$-650	1:1.5	5	72.2	30	This work

4. Conclusions

In this study, the disordered $ZnAl_2O_4$ catalysts were successfully prepared by using the citrate complex method at different temperatures ranging from 550 °C to 850 °C. The $ZnAl_2O_4$-550 catalyst exhibited a more disordered $ZnAl_2O_4$ structure than the other catalysts calcined at a higher calcination temperature, resulting in more disordered sites of AlO_4 and more oxygen vacancies in $ZnAl_2O_4$-550. The $ZnAl_2O_4$-650 catalyst having Al^{3+} cations at the octahedral sites (AlO_6) exhibited low acidity, whereas the AlO_4 sites in $ZnAl_2O_4$-550 resulted in high surface acidity. From the XPS intensities of O_a (H_2O or O_2 adsorbed) and O_b (oxygen vacancies), $ZnAl_2O_4$-550 contained more surface oxygen vacancies than $ZnAl_2O_4$-650, which contributed to the increased surface acidity of $ZnAl_2O_4$-550. The high surface acidity of $ZnAl_2O_4$-550 resulted in strong interactions with the Zn NCO complex on its surface, improving catalytic performance. The intermediate product of urea glycerolysis was 2,3-dihydroxypropyl carbamate (2), which had higher selectivity for $ZnAl_2O_4$-650 than $ZnAl_2O_4$-550, lowering the GC yield.

Supplementary Materials: The following supporting information can be downloaded at https://www.mdpi.com/article/10.3390/nano13131901/s1, Figure S1. A schematic diagram of the catalyst activity test device with the gas chromatographic analysis conditions; Figure S2: N_2 adsorption–desorption isotherms (A) and pore size distribution curves (B): (a) $ZnAl_2O_4$-550, (b) $ZnAl_2O_4$-650, (c) $ZnAl_2O_4$-750, and (d) $ZnAl_2O_4$-850; Figure S3: DTGA curves of $ZnAl_2O_4$ xerogel precursor prepared by using polymeric citrate complex method; Figure S4: Enlarged XRD patterns of fresh catalysts: (a) $ZnAl_2O_4$-550, (b) $ZnAl_2O_4$-650, (c) Znl_2O_4-750, and (d) $ZnAl_2O_4$-850; Figure S5: NH_3 profiles of fresh catalysts: (a) $ZnAl_2O_4$-550, (b) $ZnAl_2O_4$-650, (c) $ZnAl_2O_4$-750, and (d) $ZnAl_2O_4$-850; Figure S6: Typical gas chromatograms of $ZnAl_2O_4$-550 (A) and $ZnAl_2O_4$-650 (B). (2): 2,3-dihydroxypropyl carbamate, (4): 4-(hydroxymethyl) oxazolidine-2-one, and (5): (2-oxo-1,3-dioxolan-4-yl) methyl carbamate; Figure S7: CO_2 profiles of fresh catalysts: (a) $ZnAl_2O_4$-550, (b) $ZnAl_2O_4$; Table S1: The initial amount of each reactant; the amount of glycerol and products after reaction and carbon balance.

Author Contributions: H.N.-P.: methodology, validation, investigation; N.P.-N.: data curation, writing—original draft preparation; E.W.S.: conceptualization, writing—review and editing, supervision. All authors have read and agreed to the published version of the manuscript.

Funding: This research was supported by the Core Research Institute Basic Science Research Program (2021R1A6A1A03038858) and "Regional Innovation Strategy program" (No. 2021RIS-003) through the National Research Foundation of Korea (NRF) funded by the Ministry of Education and the National Research Foundation of Korea (NRF) grant funded by the Korea government (MIST) (No. 2021R1A2B5B01001448).

Data Availability Statement: The data presented in this study are available on request from the corresponding author.

Conflicts of Interest: The authors declare no conflict of interest.

References

1. Abbaszaadeh, A.; Ghobadian, B.; Omidkhah, M.R.; Najafi, G. Current biodiesel production technologies: A comparative review. *Energy Convers. Manag.* **2012**, *63*, 138–148. [CrossRef]
2. Ambat, I.; Srivastava, V.; Sillanpää, M. Recent advancement in biodiesel production methodologies using various feedstock: A review. *Renew. Sustain. Energy Rev.* **2018**, *90*, 356–369. [CrossRef]
3. Fan, X.; Burton, R.; Zhou, Y. Glycerol (byproduct of biodiesel production) as a source for fuels and chemicals mini review. *Open Fuels Ener. Sci. J.* **2010**, *3*, 17–22. [CrossRef]
4. Ochoa-Gómez, J.R.; Gómez-Jiménez-Aberasturi, O.; Ramirez-Lopez, C.; Belsué, M. A brief review on industrial alternatives for the manufacturing of glycerol carbonate, a green chemical. *Org. Process Res. Dev.* **2012**, *16*, 389–399. [CrossRef]
5. Christy, S.; Noschese, A.; Lomeli-Rodriguez, M.; Greeves, N.; Lopez-Sanchez, J.A. Recent progress in the synthesis and applications of glycerol carbonate. *Curr. Opin. Green Sustain. Chem.* **2018**, *14*, 99–107. [CrossRef]
6. Teng, W.K.; Ngoh, G.C.; Yusoff, R.; Aroua, M.K. A review on the performance of glycerol carbonate production via catalytic transesterification: Effects of influencing parameters. *Energy Convers. Manag.* **2014**, *88*, 484–497. [CrossRef]
7. Sonnati, M.O.; Amigoni, S.; de Givenchy, E.P.T.; Darmanin, T.; Choulet, O.; Guittard, F. Glycerol carbonate as a versatile building block for tomorrow: Synthesis, reactivity, properties and applications. *Green Chem.* **2013**, *15*, 283–306. [CrossRef]
8. Ochoa-Gómez, J.R.; Gómez-Jiménez-Aberasturi, O.; Maestro-Madurga, B.; Pesquera-Rodríguez, A.; Ramírez-López, C.; Lorenzo-Ibarreta, L.; Torrecilla-Soria, J.; Villarán-Velasco, M.C. Synthesis of glycerol carbonate from glycerol and dimethyl carbonate by transesterification: Catalyst screening and reaction optimization. *Appl. Catal. A Gen.* **2009**, *366*, 315–324. [CrossRef]
9. Song, X.; Pan, D.; Wu, Y.; Cheng, P.; Wei, R.; Gao, L.; Zhang, J.; Xiao, G. Synthesis of glycerol carbonate over porous La-Zr based catalysts: The role of strong and super basic sites. *J. Alloys Compd.* **2018**, *750*, 828–837. [CrossRef]
10. Devarajan, A.; Thiripuranthagan, S.; Radhakrishnan, R.; Kumaravel, S. Solvent free transesterification of glycerol into glycerol carbonate over nanostructured CaAl hydrotalcite catalyst. *J. Nanosci. Nanotechnol.* **2018**, *18*, 4588–4599. [CrossRef] [PubMed]
11. Li, Y.; Liu, J.; He, D. Catalytic synthesis of glycerol carbonate from biomass-based glycerol and dimethyl carbonate over Li-La_2O_3 catalysts. *Appl. Catal. A Gen.* **2018**, *564*, 234–242. [CrossRef]
12. Li, Q.; Zhang, W.; Zhao, N.; Wei, W.; Sun, Y. Synthesis of cyclic carbonates from urea and diols over metal oxides. *Catal. Today* **2006**, *115*, 111–116. [CrossRef]
13. Park, C.-y.; Nguyen-Phu, H.; Shin, E.W. Glycerol carbonation with CO_2 and $La_2O_2CO_3$/ZnO catalysts prepared by two different methods: Preferred reaction route depending on crystalline structure. *Mol. Catal.* **2017**, *435*, 99–109. [CrossRef]
14. Song, X.; Wu, Y.; Pan, D.; Zhang, J.; Xu, S.; Gao, L.; Wei, R.; Xiao, G. Functionalized DVB-based polymer catalysts for glycerol and CO_2 catalytic conversion. *J. CO_2 Util.* **2018**, *28*, 326–334. [CrossRef]
15. Nguyen-Phu, H.; Park, C.-y.; Eun, W.S. Activated red mud-supported Zn/Al oxide catalysts for catalytic conversion of glycerol to glycerol carbonate: FTIR analysis. *Catal. Commun.* **2016**, *85*, 52–56. [CrossRef]
16. Nguyen-Phu, H.; Shin, E.W. Disordered structure of $ZnAl_2O_4$ phase and the formation of a Zn NCO complex in ZnAl mixed oxide catalysts for glycerol carbonylation with urea. *J. Catal.* **2019**, *373*, 147–160. [CrossRef]
17. Nguyen-Phu, H.; Park, C.-y.; Shin, E.W. Dual catalysis over ZnAl mixed oxides in the glycerolysis of urea: Homogeneous and heterogeneous reaction routes. *Appl. Catal. A Gen.* **2018**, *552*, 1–10. [CrossRef]
18. Fujita, S.-i.; Yamanishi, Y.; Arai, M. Synthesis of glycerol carbonate from glycerol and urea using zinc-containing solid catalysts: A homogeneous reaction. *J. Catal.* **2013**, *297*, 137–141. [CrossRef]
19. Chen, L.; Sun, X.; Liu, Y.; Zhou, K.; Li, Y. Porous $ZnAl_2O_4$ synthesized by a modified citrate technique. *J. Alloys Compd.* **2004**, *376*, 257–261.
20. Sotomayor, F.J.; Cychosz, K.A.; Thommes, M. Characterization of micro/mesoporous materials by physisorption: Concepts and case studies. *Acc. Mater. Surf. Res.* **2018**, *3*, 34–50.
21. Tangcharoen, T.; T-Thienprasert, J.; Kongmark, C. Effect of calcination temperature on structural and optical properties of MAl_2O_4 (M = Ni, Cu, Zn) aluminate spinel nanoparticles. *J. Adv. Ceram.* **2019**, *8*, 352–366. [CrossRef]
22. Holzwarth, U.; Gibson, N. The Scherrer equation versus the 'Debye-Scherrer equation'. *Nat. Nanotechnol.* **2011**, *6*, 534. [CrossRef]
23. Dwibedi, D.; Murugesan, C.; Leskes, M.; Barpanda, P. Role of annealing temperature on cation ordering in hydrothermally prepared zinc aluminate ($ZnAl_2O_4$) spinel. *Mater. Res. Bull.* **2018**, *98*, 219–224. [CrossRef]
24. Simeone, D.; Dodane-Thiriet, C.; Gosset, D.; Daniel, P.; Beauvy, M. Order–disorder phase transition induced by swift ions in $MgAl_2O_4$ and $ZnAl_2O_4$ spinels. *J. Nucl. Mater.* **2002**, *300*, 151–160. [CrossRef]

25. Barpanda, P.; Behera, S.; Gupta, P.; Pratihar, S.; Bhattacharya, S. Chemically induced order disorder transition in magnesium aluminium spinel. *J. Eur. Ceram. Soc.* **2006**, *26*, 2603–2609. [CrossRef]
26. Da Silva, A.A.; Gonçalves, A.d.S.; Davolos, M.R. Characterization of nanosized $ZnAl_2O_4$ spinel synthesized by the sol–gel method. *J. Sol-Gel Sci. Technol.* **2009**, *49*, 101–105. [CrossRef]
27. Busca, G.; Lorenzelli, V.; Escribano, V.S.; Guidetti, R. FT-113 study of the surface properties of the spinels $NiAl_2O_4$ and $CoAl_2O_4$ in relation to those of transitional aluminas. *J. Catal.* **1991**, *131*, 167–177. [CrossRef]
28. Morterra, C.; Magnacca, G. A case study: Surface chemistry and surface structure of catalytic aluminas, as studied by vibrational spectroscopy of adsorbed species. *Catal. Today* **1996**, *27*, 497–532. [CrossRef]
29. Menon, S.G.; Choudhari, K.S.; Shivashankar, S.A.; Chidangil, S.; Kulkarni, S.D. Microwave solution route to ceramic $ZnAl_2O_4$ nanoparticles in 10 minutes: Inversion and photophysical changes with thermal history. *New J. Chem.* **2017**, *41*, 5420–5428. [CrossRef]
30. Duan, X.; Yuan, D.; Yu, F. Cation distribution in Co-doped $ZnAl_2O_4$ nanoparticles studied by X-ray photoelectron spectroscopy and 27Al solid-state NMR spectroscopy. *Inorg. Chem.* **2011**, *50*, 5460–5467. [CrossRef]
31. Tshabalala, K.; Cho, S.-H.; Park, J.-K.; Pitale, S.S.; Nagpure, I.; Kroon, R.; Swart, H.; Ntwaeaborwa, O. Luminescent properties and X-ray photoelectron spectroscopy study of $ZnAl_2O_4$: Ce^{3+}, Tb^{3+} phosphor. *J. Alloys Compd.* **2011**, *509*, 10115–10120. [CrossRef]
32. Druska, P.; Steinike, U.; Šepelák, V. Surface structure of mechanically activated and of mechanosynthesized zinc ferrite. *J. Solid State Chem.* **1999**, *146*, 13–21. [CrossRef]
33. Jayathilake, D.; Peiris, T.N.; Sagu, J.S.; Potter, D.B.; Wijayantha, K.; Carmalt, C.; Southee, D. Microwave-assisted synthesis and processing of Al-doped, Ga-doped, and Al, Ga codoped ZnO for the pursuit of optimal conductivity for transparent conducting film fabrication. *ACS Sustain. Chem. Eng.* **2017**, *5*, 4820–4829. [CrossRef]
34. Chen, M.; Wang, X.; Yu, Y.; Pei, Z.; Bai, X.; Sun, C.; Huang, R.; Wen, L. X-ray photoelectron spectroscopy and auger electron spectroscopy studies of Al-doped ZnO films. *Appl. Surf. Sci.* **2000**, *158*, 134–140. [CrossRef]
35. Murthy, I.; Swamy, C. Catalytic decomposition of 2-propanol on $Co_{1+x}Al_{2-x}O_4$ spinel system. *Catal. Lett.* **1994**, *27*, 103–112. [CrossRef]
36. Busca, G.; Lorenzelli, V.; Ramis, G.; Willey, R.J. Surface sites on spinel-type and corundum-type metal oxide powders. *Langmuir* **1993**, *9*, 1492–1499. [CrossRef]
37. Lundie, D.T.; McInroy, A.R.; Marshall, R.; Winfield, J.M.; Jones, P.; Dudman, C.C.; Parker, S.F.; Mitchell, C.; Lennon, D. Improved description of the surface acidity of η-alumina. *J. Phys. Chem. B* **2005**, *109*, 11592–11601. [CrossRef]
38. Trombetta, M.; Busca, G.; Lenarda, M.; Storaro, L.; Ganzerla, R.; Piovesan, L.; Lopez, A.J.; Alcantara-Rodrìguez, M.; Rodríguez-Castellón, E. Solid acid catalysts from clays: Evaluation of surface acidity of mono-and bi-pillared smectites by FT-IR spectroscopy measurements, NH3-TPD and catalytic tests. *Appl. Catal. A Gen.* **2000**, *193*, 55–69.
39. Sohlberg, K.; Pantelides, S.T.; Pennycook, S.J. Surface Reconstruction and the Difference in Surface Acidity between γ- and η-Alumina. *J. Am. Chem. Soc.* **2001**, *123*, 26–29. [CrossRef]
40. Mefford, J.T.; Hardin, W.G.; Dai, S.; Johnston, K.P.; Stevenson, K.J. Anion charge storage through oxygen intercalation in $LaMnO_3$ perovskite pseudocapacitor electrodes. *Nat. Mater.* **2014**, *13*, 726–732. [CrossRef]
41. Turney, T.W.; Patti, A.; Gates, W.; Shaheen, U.; Kulasegaram, S. Formation of glycerol carbonate from glycerol and urea catalysed by metal monoglycerolates. *Green Chem.* **2013**, *15*, 1925–1931. [CrossRef]
42. Lu, F.; Song, B.; He, P.; Wang, Z.; Wang, J. Electrochemical impedance spectroscopy (EIS) study on the degradation of acrylic polyurethane coatings. *RSC Adv.* **2017**, *7*, 13742–13748. [CrossRef]
43. Fernandes, G.P.; Yadav, G.D. Selective glycerolysis of urea to glycerol carbonate using combustion synthesized magnesium oxide as catalyst. *Catal. Today* **2018**, *309*, 153–160. [CrossRef]
44. Zhang, P.; Liu, L.; Fan, M.; Dong, Y.; Jiang, P. The value-added utilization of glycerol for the synthesis of glycerol carbonate catalyzed with a novel porous ZnO catalyst. *RSC Adv.* **2016**, *6*, 76223–76230. [CrossRef]
45. Rubio-Marcos, F.; Calvino-Casilda, V.; Bañares, M.A.; Fernandez, J.F. Control of the interphases formation degree in Co_3O_4/ZnO catalysts. *ChemCatChem* **2013**, *5*, 1431–1440. [CrossRef]
46. Zhang, J.; He, D. Lanthanum-based mixed oxides for the synthesis of glycerol carbonate from glycerol and urea. *React. Kinet. Mech. Catal.* **2014**, *113*, 375–392. [CrossRef]
47. Procopio, D.; Di Gioia, M.L. An overview of the latest advances in the catalytic synthesis of glycerol carbonate. *Catalysts* **2022**, *12*, 50. [CrossRef]
48. Mallesham, B.; Rangaswamy, A.; Rao, B.G.; Rao, T.V.; Reddy, B.M. Solvent-free production of glycerol carbonate from bioglycerol with urea over nanostructured promoted SnO_2 catalysts. *Catal. Lett.* **2020**, *150*, 3626–3641. [CrossRef]
49. Nguyen-Phu, H.; Shin, E.W. Investigating time-dependent Zn species over Zn-based catalysts in glycerol carbonylation with urea and their roles in the reaction mechanism. *Appl. Catal. A Gen.* **2018**, *561*, 28–40. [CrossRef]
50. Chen, J.; Wang, C.; Dong, B.; Leng, W.; Huang, J.; Ge, R.; Gao, Y. Ionic liquids as eco-friendly catalysts for converting glycerol and urea into high value-added glycerol carbonate. *Chin. J. Catal.* **2015**, *36*, 336–343. [CrossRef]